

Spin-1 Haldane chains of superconductor-semiconductor hybridsVirgil V. Baran^{1,2,3,*} and Jens Paaske³¹*Faculty of Physics, University of Bucharest, 405 Atomistilor, RO-077125, Bucharest-Măgurele, Romania*²*“Horia Hulubei” National Institute of Physics and Nuclear Engineering, 30 Reactorului, RO-077125, Bucharest-Măgurele, Romania*³*Center for Quantum Devices, Niels Bohr Institute, University of Copenhagen, 2100 Copenhagen, Denmark*

(Received 23 April 2024; revised 12 July 2024; accepted 15 July 2024; published 1 August 2024)

We theoretically explore the possibility of realizing the symmetry-protected topological Haldane phase of spin-1 chains in a tunable hybrid platform of superconducting islands (SIs) and quantum dots (QDs). Inspired by recent findings suggesting that an appropriately tuned QD-SI-QD block may behave as a robust spin-1 unit, we study the behavior of many such units tunnel-coupled into linear chains. Our efficient and fully microscopic modeling of long chains with several tens of units is enabled by the use of the surrogate model solver [V. V. Baran *et al.*, *Phys. Rev. B* **108**, L220506 (2023); **109**, 224501 (2024)]. Our numerical findings indicate that the QD-SI-QD chains exhibit emblematic features of the Haldane phase, such as fractional spin-1/2 edge states and nonvanishing string order parameters, and that these persist over a sizable region of parameter space.

DOI: [10.1103/PhysRevB.110.064503](https://doi.org/10.1103/PhysRevB.110.064503)**I. INTRODUCTION**

Fueled by open problems in both fundamental and applied physics, the field of superconductor-semiconductor hybrids has witnessed sustained advances over the past few decades. Crucial to the understanding of these super-semi systems is the hybridization between their various constituents, which often leads to the presence of tunable subgap states [1–7]. Their properties directly influence the design of superconducting qubits and other complex gateable devices for quantum technologies [8–10].

In particular, the ongoing efforts of realizing poor man’s Majorana bound states in short Kitaev chains [11–18] rely on the hybridization of two spatially separated quantum dots (QDs) with an extended gateable super-semi subgap state. A closely related configuration, where the two QDs are coupled through a floating superconducting island (SI), was recently considered for its interesting exchange properties [19,20]. Remarkably, it turns out that the QD-SI-QD (DSD) exhibits a robust spin-1 ground state when the QDs couple strongly and coherently through (at least two subgap states in) the SI, in the presence of a sizable SI Coulomb energy [20]. Inspired by this finding, we explore here the possibility of realizing the well-known Haldane phase of spin-1 chains in this super-semi hybrid platform.

The Haldane phase is a celebrated symmetry-protected topological phase of matter realized in the gapped ground state of the spin-1 antiferromagnetic Heisenberg chain [21–25]. The hallmark of such phases is the existence of particular edge modes which enjoy some degree of topological protection, i.e., they are robust to symmetry-preserving local perturbations. The Haldane phase of a long-enough spin-1 chain with open boundary conditions features a fourfold-degenerate

many-body ground state with the edge modes behaving as two effective spin-1/2 degrees of freedom despite the fact that the model’s elementary building blocks were spins-1. This symmetry *fractionalization* phenomenon [26] is well-illustrated by the analytical valence bond solid solution of the Affleck-Kennedy-Lieb-Tasaki (AKLT) model [27].

The existence of edge states in spin-1 chains has been extensively investigated over the past decades, both theoretically [28–30] and experimentally [31–36]. Various platforms for realizing synthetic spin-1 chains have been proposed over the years, e.g., by using gated triple quantum dots [37], arrays of semiconductor QDs in a nanowire [38–40], a chain of triangular graphene QDs [41,42], in addition to molecular [43] and organometallic platforms [44–47]. Various applications of the spin-1/2 edge states as qubits have also been suggested [37,38,48]. Furthermore, they have direct implications for measurement-based quantum computation [49,50].

The purpose of this work is to show that the Haldane phase may also be realized in a tunable DSD chain under experimentally reasonable assumptions. The rest of the paper is organized as follows. In Sec. II, we lay down the modeling methodology based on the surrogate model solver [20,51]. Furthermore, we introduce the Heisenberg Hamiltonian and its bilinear-biquadratic generalization as ideal spin-1 chains to be used as benchmarks for the DSD results. In Sec. III, we discuss the numerical results (energy spectra, spin-densities, string order parameters) obtained for DSD chains of increasing length: the individual unit ($N = 1$), the dimer ($N = 2$), intermediate length chains ($N = 3, \dots, 12$), and finally long chains ($N = 21, 41$), which are expected to visibly display the main features of the Haldane phase. We draw conclusions and discuss possible generalizations of our work in Sec. IV.

*Contact author: virgil.v.baran@unibuc.ro

II. MODELING METHODOLOGY

A. DSD chains

The total Hamiltonian for a length- N DSD chain is given by

$$\hat{H} = \sum_{n=1}^N \hat{H}_{\text{DSD},n} + t_d \sum_{n=1}^{N-1} \sum_{\sigma=\uparrow\downarrow} (d_{nR\sigma}^\dagger d_{n+1,L,\sigma} + \text{H.c.}), \quad (1)$$

where $d_{n\alpha\sigma}^\dagger$ creates an electron with spin σ in the $\alpha = \text{L,R}$ quantum dot of the n th DSD unit. We consider all units to be identical and described by a Hamiltonian of the form

$$\hat{H}_{\text{DSD}} = \hat{H}_{\text{QD,L}} + \hat{H}_{\text{SI}} + \hat{H}_{\text{QD,R}} + \hat{H}_{\text{tunn}}. \quad (2)$$

For each quantum dot $\alpha = \text{L,R}$ we use the constant interaction Hamiltonian

$$\hat{H}_{\text{QD},\alpha} = \epsilon_d (d_{\alpha\uparrow}^\dagger d_{\alpha\uparrow} + d_{\alpha\downarrow}^\dagger d_{\alpha\downarrow}) + U d_{\alpha\uparrow}^\dagger d_{\alpha\uparrow} d_{\alpha\downarrow}^\dagger d_{\alpha\downarrow}, \quad (3)$$

where U is the electron-electron repulsion strength and ϵ_d is the dot energy level. Throughout this work, we assume all QDs to be identical, with $\epsilon_d = -U/2$. Departing from this particle-hole symmetric point is known to reduce the excitation gap above the spin-1 DSD ground state of interest here [19]. Furthermore, we neglect any cross capacitances between the different parts of the DSD units, the effects of which can be accounted for by rescaling the various parameters.

For modeling the SI and its tunnel couplings, we employ the surrogate model solver (SMS) methodology outlined in Refs. [20,51]. For a vanishing SI charging energy E_c , the full quasicontinuum of SI levels is replaced within the SMS approach by a small number \tilde{L} of BCS surrogate orbitals that optimally reproduce the SI-QD hybridization function [51]. The SMS approach may be generalized to a nonvanishing E_c provided that the finite-size effects of the SI can safely be neglected [20]. In this case, the SMS prescription consists of coupling the BCS surrogate orbitals (used as before to model the hybridization part) with an auxiliary Cooper pair counting site that enables the conservation of the total SI particle number. This leads to an accurate description of the SI's charge fluctuations and thus ensures a proper treatment of its Coulomb interaction term. Concretely, the SI Hamiltonian is given by

$$\begin{aligned} \hat{H}_{\text{SI}} = & \sum_{\ell=1}^{\tilde{L}} \sum_{\sigma=\uparrow\downarrow} \tilde{\xi}_\ell c_{\ell\sigma}^\dagger c_{\ell\sigma} - \sum_{\ell=1}^{\tilde{L}} (\Delta c_{\ell\uparrow}^\dagger c_{\ell\downarrow}^\dagger e^{-i\hat{\phi}} + \text{H.c.}) \\ & + E_c \left(\sum_{\ell=1}^{\tilde{L}} \sum_{\sigma=\uparrow\downarrow} c_{\ell\sigma}^\dagger c_{\ell\sigma} + 2\hat{N}_p - n_0 \right)^2. \end{aligned} \quad (4)$$

Here $c_{\ell\sigma}^\dagger$ creates an electron with spin σ and energy $\tilde{\xi}_\ell$ in the SI with charging energy E_c and optimal occupation (in units of electron charge) n_0 . As discussed above, we need to make use of the canonically conjugate number and phase operators \hat{N}_p and $\hat{\phi}$, $[\hat{N}_p, e^{i\hat{\phi}}] = e^{i\hat{\phi}}$. Physically, \hat{N}_p counts the number of Cooper pairs in the superconducting condensate, while $e^{\pm i\hat{\phi}}$ adds/removes one pair from the condensate. The auxiliary

Hilbert space is spanned by states $|p\rangle$ with an integer number of pairs p , obeying $\hat{N}_p|p\rangle = p|p\rangle$ and $e^{\pm i\hat{\phi}}|p\rangle = |p \pm 1\rangle$.

Finally, the QD-SI coupling term appearing in Eq. (2) reads

$$\hat{H}_{\text{tunn}} = \sum_{\alpha=\text{L,R}} \sum_{\ell=1}^{\tilde{L}} \sum_{\sigma=\uparrow\downarrow} \sqrt{\gamma_\ell \Gamma_\alpha} (c_{\ell\sigma}^\dagger d_{\alpha\sigma} + \text{H.c.}), \quad (5)$$

where Γ_α denote the QD $_\alpha$ -SI tunneling rates. The γ_ℓ parameters define the surrogate model, together with the energy levels $\tilde{\xi}_\ell$.

As detailed in Ref. [20], the minimal prescription for reproducing the spin-1 ground state of the DSD unit relies on the $\tilde{L} = 2$ surrogate. This is also in agreement with Ref. [19], where a finite-bandwidth was found to be essential for this purpose (see also Appendix A for a complementary discussion). For the minimal $\tilde{L} = 2$ surrogate employed throughout this work, the numerical values of the above parameters are $\gamma_{1,2} = 1.246\Delta$ and $\tilde{\xi}_{1,2} = \pm 1.31\Delta$ (obtained by the optimization method detailed in Ref. [51] for a half-bandwidth $D = 10\Delta$). For these values, the excitation energy of the BCS quasiparticles becomes $E_{\text{qp}} = (\Delta^2 + \tilde{\xi}^2)^{1/2} \simeq 1.65\Delta$. In the best-case scenario considered here with the QDs symmetrically coupled to the SI, the more complex surrogates with $\tilde{L} \geq 3$ effective levels in the SI are known to converge towards a slightly larger spin-singlet-triplet gap for the DSD unit [20]. They are found, however, to cause only minor quantitative differences for the DSD chains considered below. More general surrogate models could be formulated in order to account for the variability in the couplings of each QD to the SI due to the mesoscopic randomness of the system [52], as will be considered in future works.

B. Mapping to ideal spin-1 chains

When the interdot coupling t_d is small enough and the picture of robust spin-1 DSD units holds, the low-energy spectrum of \hat{H} in Eq. (1) may be matched to that of the spin-1 antiferromagnetic Heisenberg chain (AFH) given by

$$\hat{H}_{\text{AFH}} = J_{\text{AF}} \sum_{i=1}^{N-1} \vec{S}_i \cdot \vec{S}_{i+1}, \quad (6)$$

with the coupling $J_{\text{AF}} > 0$ following the superexchange scaling [53] $J_{\text{AF}} \sim t_d^2/U$. The spin-1 character of each DSD unit is gradually lost with increasing t_d as the correlations between QDs belonging to neighboring units build up [see also Figs. 3(a) and 5(b) below].

The large- t_d limit corresponds to a dimerized configuration where all double-dots are effectively locked into spin-singlet configurations [see Fig. 1(b)], leaving two isolated (dangling) spin-1/2 moments at the chain's edges. Naively, this behavior would appear reminiscent of the AKLT ansatz in which every spin-1 is identified with the triplet subspace of two virtual spins-1/2 each participating in a singlet bond with its other neighboring spin [27]. The AKLT state is the ground state of the bilinear-biquadratic (BLBQ) Hamiltonian

$$\hat{H}_{\text{BLBQ}} = J_{\text{AF}} \sum_{i=1}^{N-1} [\vec{S}_i \cdot \vec{S}_{i+1} + \beta (\vec{S}_i \cdot \vec{S}_{i+1})^2] \quad (7)$$

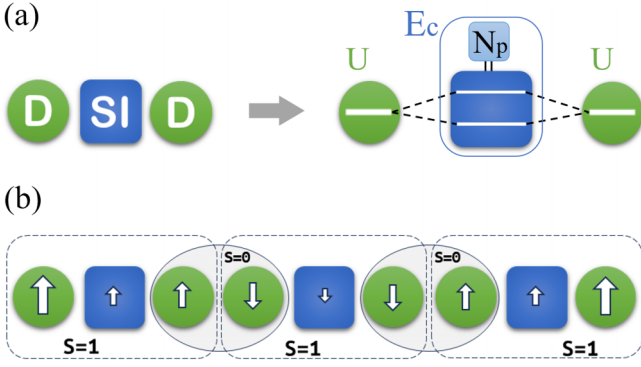


FIG. 1. (a) Modeling of the DSD unit in the SMS approach with a minimal $\tilde{L} = 2$ surrogate for the SI coupled to an auxiliary site counting the number of Cooper pairs N_p in the superconducting condensate. (b) Schematic of the $N = 3$ DSD chain in its $S_{\text{tot}} = S_{z,\text{tot}} = 1$ ground state. The strength of the $S = 0$ valence bond is dictated by the interdot tunnel matrix element t_d ; see Eq. (1).

for $\beta_{\text{AKLT}} = 1/3$. For this particular value of β , \hat{H}_{BLBQ} becomes a sum of projectors onto local spin-2 pairs, which thus favors the formation of spin-singlet valence bonds (in the picture of the spin-1 consisting of two symmetrized virtual spins-1/2). Note that the biquadratic exchange coupling is also the simplest local term that is compatible with all the system's symmetries which may be added to the Heisenberg Hamiltonian of Eq. (6). The BLBQ model features both gapped excitations and fractional spin-1/2 edge states, with a fourfold degeneracy in the thermodynamic limit, in a range that includes $\beta \in (0, 1/3)$, which resides well within the Haldane phase given by $\beta \in (-1, 1)$ [28,54].

In the following section, we will argue that the low-energy physics of the DSD chains (at weak enough t_d) is well captured by the BLBQ Hamiltonian of Eq. (7) with $\beta \in (0, 1/3)$, and satisfies the necessary requirements of the Haldane phase.

III. RESULTS

To obtain the low-lying spectrum of the quasi-1D and locally interacting systems considered here, our numerical method of choice is the density matrix renormalization group (DMRG) in the matrix-product-state formulation [55,56]. We collect in Appendix B the technical details regarding our simulations.

A. The DSD unit

Let us first briefly revisit the elementary QD-SI-QD (DSD) unit, whose properties have been investigated in some detail in Refs. [19,20]. The emergence of the spin-triplet ground state in this setup may be understood in analogy to the double-dot configuration of Ref. [57]. In a perturbative approach, in addition to the hybridization between the QDs' spin-singlet and the Cooper pairs (that would naively lead to an overall singlet ground state), one must consider fourth-order tunneling processes involving single-particle excitations in the superconducting leads. When it becomes advantageous to perform the spin-exchange by virtually exciting the superconductor instead of the QDs, a spin-triplet ground state may emerge, as detailed in Appendix A and in Ref. [57].

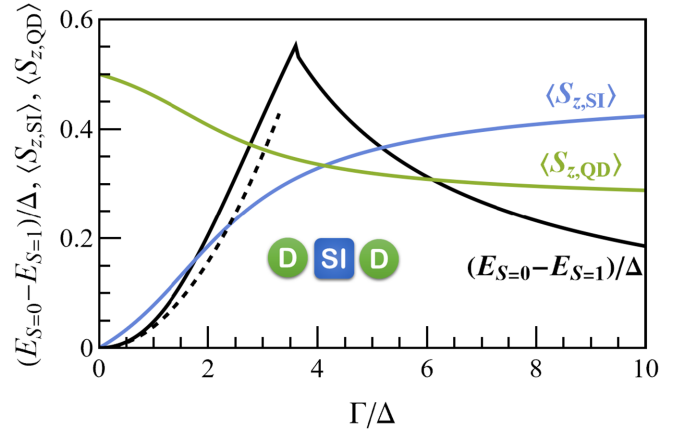


FIG. 2. DSD spin-singlet-triplet energy gap and average SI and QD spins $\langle S_z \rangle$ in the $S_{\text{tot}} = S_{z,\text{tot}} = 1$ ground state. The dashed line indicates the spin-singlet-triplet gap obtained by perturbation theory (see Appendix A). The other parameters are $U = -2\epsilon_d = 6\Delta$, $E_c = 2\Delta$. For the SI we employed the $\tilde{L} = 2$ surrogate.

In modeling the DSD unit, we implicitly assumed that the QDs are coupled through the *same* SI-orbitals, much like in the poor man's Majorana devices where a spatially extended state in the proximitized semiconductor allows for crossed Andreev reflections [13–15]. Also, it is important to note that the spin-triplet character of the QD-SI-QD system is rather sensitive to the asymmetry in the magnitude of the couplings between the QD and superconducting levels (see the discussion around Fig. 8 of Ref. [20]). Furthermore, due to the two-orbital structure of the SI there is a leftover phase from the four tunneling amplitudes that cannot be gauged away and which may impact negatively on the robustness of the spin-triplet. Altogether, this makes the basic DSD units vulnerable to mesoscopic fluctuations, which seem hard to circumvent with gate-defined quantum dots and islands. At this point, we can only speculate that fluctuations could be reduced by moving to a super-semi hybrid platform based on highly regular epitaxially grown tunnel barriers [58–60]. Henceforth, we will assume the best-case scenario of symmetric couplings within the DSD unit and focus on the physics that would emerge from assembling many such units into longer chains.

We show in Fig. 2 the behavior of the DSD unit's spin-singlet-triplet gap with increasing QD-SI tunneling rate Γ , which shows a robust maximum corresponding to the crossing between the two lowest-lying spin-singlet states. This maximum is located at $\Gamma \simeq 3.5\Delta$ and reaches around 0.6Δ for $\tilde{L} = 2$ (converging to a slightly larger value for $\tilde{L} \geq 3$ surrogates). At zero coupling, the difference between the lowest-lying spin singlets is the presence of a broken Cooper pair with an energy cost of $2E_{\text{qp}}$. This becomes favored by a strong enough tunneling rate that encourages the states with single QD occupation to hybridize with the SC quasiparticle excitations (and also allows for empty/doubly occupied QDs).

Furthermore, Fig. 2 indicates that in the hybridization regime where the DSD's spin-triplet character is the most robust, the QD and SI components contribute democratically to the total spin $S = 1$. The physical picture is that of a highly correlated DSD unit, fundamentally different from

the weak QD-SI coupling scenario where each QD carries a well-defined spin-1/2 moment. For weak QD-SI couplings, the DSD chain would thus map well to the alternating ferromagnetic-antiferromagnetic Heisenberg chain of spins-1/2. With increasing antiferromagnetic coupling (the analog of the interdot coupling t_d), this model is known to experience a continuous crossover between the Haldane phase and a dimerized phase [61,62].

B. The DSD-DSD dimer

Moving on to the simplest DSD chain, i.e., the $N = 2$ dimer, we focus on its lowest lying total-spin-singlet, triplet, and quintuplet states, indicated by different colors in Figs. 3(a)–3(c). For all cases, we confirm in Fig. 3(a) the gradual breakdown of the spin-triplet character of each DSD unit with increasing interdot coupling t_d . Here, we show each unit's effective total spin S_{DSD} defined by $S_{\text{DSD}}(S_{\text{DSD}} + 1) = \langle \vec{S}_{\text{DSD}}^2 \rangle$, together with its range of fluctuations $S_{\text{DSD}} \pm \delta S_{\text{DSD}}$ that reproduces the spread of the total spin squared between $\langle \vec{S}_{\text{DSD}}^2 \rangle \pm \sqrt{(\langle \vec{S}_{\text{DSD}}^2 \rangle)^2 - \langle \vec{S}_{\text{DSD}} \rangle^2}/2$. The total spin of each DSD unit is understood to be $\vec{S}_{\text{DSD}} = \vec{S}_{\text{QD,L}} + \vec{S}_{\text{SI}} + \vec{S}_{\text{QD,R}}$.

The behavior of the DSD-dimer's low-lying energy spectrum interpolates between the AFH-specific scaling $E_{S=1} - E_{S=0} = (E_{S=2} - E_{S=1})/2 = J_{\text{AF}}$ at low t_d , and the AKLT-like scenario with degenerate spin-singlet and -triplet ground states at large t_d (see also the discussion in Sec. II B above). For intermediate values of t_d , we use the BLBQ prescription $E_{S=1} - E_{S=0} = J_{\text{AF}}(1 - 3\beta)$, $E_{S=2} - E_{S=1} = 2J_{\text{AF}}$ to obtain the J_{AF} and β parameters of the effective BLBQ model; see Eq. (7). The fitting results are shown in Figs. 3(c) and 3(d), with the effective antiferromagnetic coupling J_{AF} following the superexchange scaling $J_{\text{AF}} \sim t_d^2/U$ to a good extent [63], and with the biquadratic term β interpolating smoothly between $\beta_{\text{AFH}} = 0$ (at small t_d) and $\beta_{\text{AKLT}} = 1/3$ (at large t_d).

C. Longer DSD chains

1. Energy spectra

When increasing to $N \geq 3$ two main signatures of the Haldane phase become manifest, namely the exponential decay of the spin-triplet-singlet gap (with alternating singlet and triplet ground states for even and odd N) and the convergence of the spin-quintuplet excitation energy to the corresponding Haldane gap; see Fig. 4. Note that a faster breakdown of the spin-triplet character is to be expected for the DSD units in the bulk of $N \geq 3$ chains, as each unit now interacts with both its left and right neighbors. This is apparent in Fig. 4, where a value of $\beta_{N=12} = 0.14$ within the BLBQ model is needed to reproduce well the DSD spin-gaps for $N = 12$, about twice as large when compared to $\beta_{N=2} \simeq 0.07$ required for the $N = 2$ DSD-dimer at the same $t_d = 0.4\Delta$; cf. also Fig. 3(d).

2. Spin densities and edge states

Even longer chains show clear signatures specific to the spin-1/2 edge fractionalization [28]; see Fig. 5(a). Here, the average spin in the $S_{\text{tot}} = S_{z,\text{tot}} = 1$ ground state of the $N = 21$ DSD chain displays the characteristic staggered profile decaying in amplitude away from the edges. This decay is correlated with the strength of the double-dot spin-singlet bonds, being

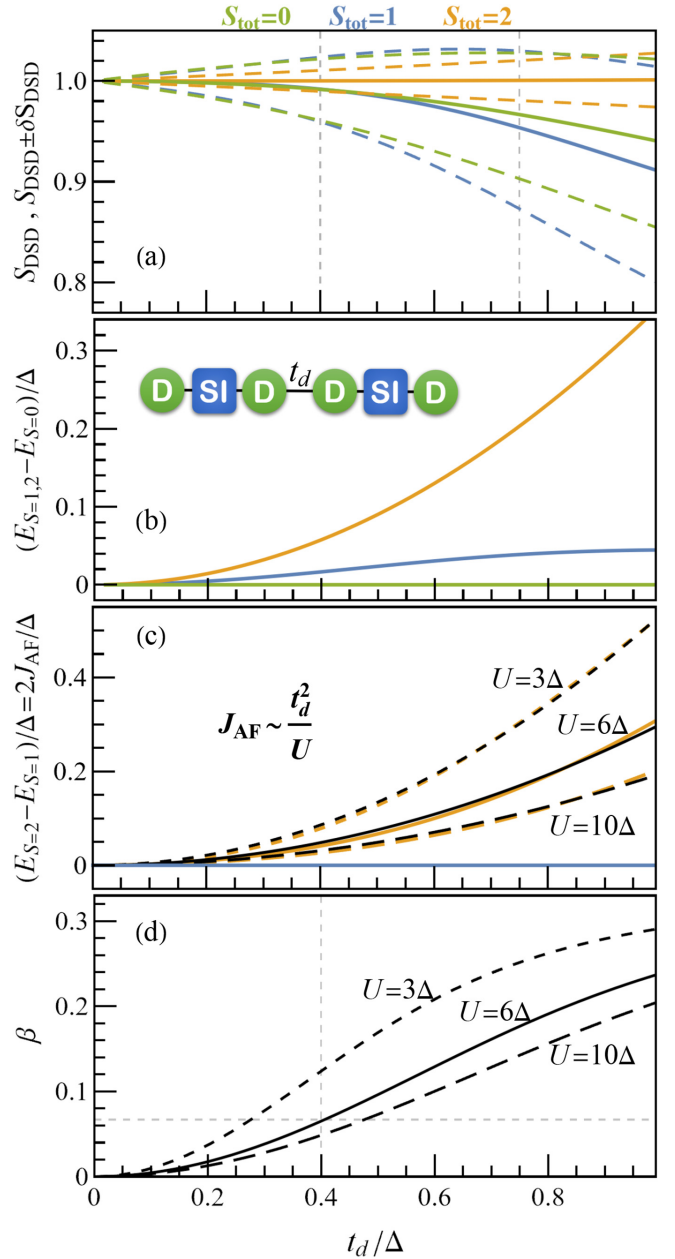


FIG. 3. (a) Effective total spin S_{DSD} (continuous lines), defined for each DSD unit by $S_{\text{DSD}}(S_{\text{DSD}} + 1) = \langle \vec{S}_{\text{DSD}}^2 \rangle$, and its estimated range of fluctuations (dashed lines) vs the interdot coupling t_d , for the $N_{\text{DSD}} = 2$ dimer in its lowest-lying $S_{\text{tot}} = 0, 1, 2$ states. (b) Spin-triplet and spin-quintuplet excitation energies vs the interdot coupling t_d . (c), (d) BLBQ parameters $J_{\text{AF}} = (E_{S=2} - E_{S=1})/2$ and β resulting from fitting the dimer's energy spectrum (black curves). For the fitting of J_{AF} , see also [63]. The values referred to in the main text are indicated by dashed grid lines. The other parameters are $U = 6\Delta$ [in (a), (b)], $\epsilon_d = -U/2$, $\Gamma = 3\Delta$, $E_c = 2\Delta$. For each SI we employed the $\tilde{L} = 2$ surrogate.

weakest at small t_d , i.e., in the AFH regime, and strongest at large t_d , i.e., in the AKLT-like dimerized regime, where only the end-spins-1/2 survive and there is no bulk magnetization. When going towards the latter regime by progressively increasing t_d , the double-dots tighten up into spin singlets and the DSD units across the entire chain experience increasingly

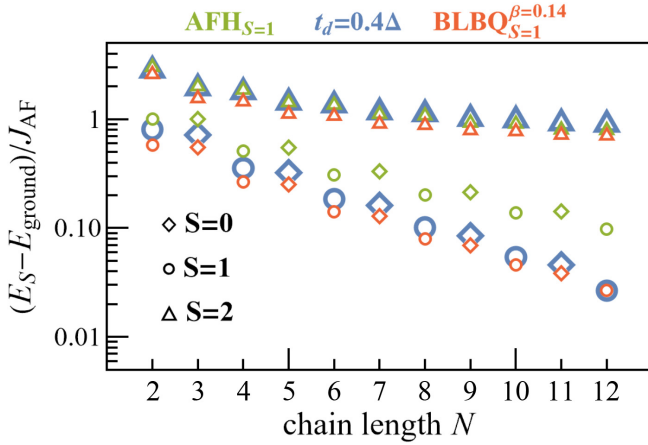


FIG. 4. Spin energy gaps for the DSD, AFH, and BLBQ($\beta = 0.14$) chains relative to the spin-singlet (triplet) ground state for even (odd) chain lengths N . The DSD chain parameters are $U = -2\epsilon_d = 6\Delta$, $\Gamma = 3\Delta$, $E_c = 2\Delta$, $t_d = 0.4\Delta$, and $J_{AF} = 0.0205\Delta$. For each SI we employed the $\tilde{L} = 2$ surrogate.

stronger fluctuations, gradually losing their spin-1 character; cf. Fig. 5(b) and see also the discussion around Fig. 3(a).

The increasing- t_d effects on the edge states are shown in Fig. 6 for a larger $N = 41$ DSD chain. In this figure only, we plot the detailed spin distribution for each individual QD and SI instead of that corresponding to entire DSD units. For small to moderate t_d , i.e., close to the AFH regime, each QD and SI is seen to contribute a similar amount to the average spin

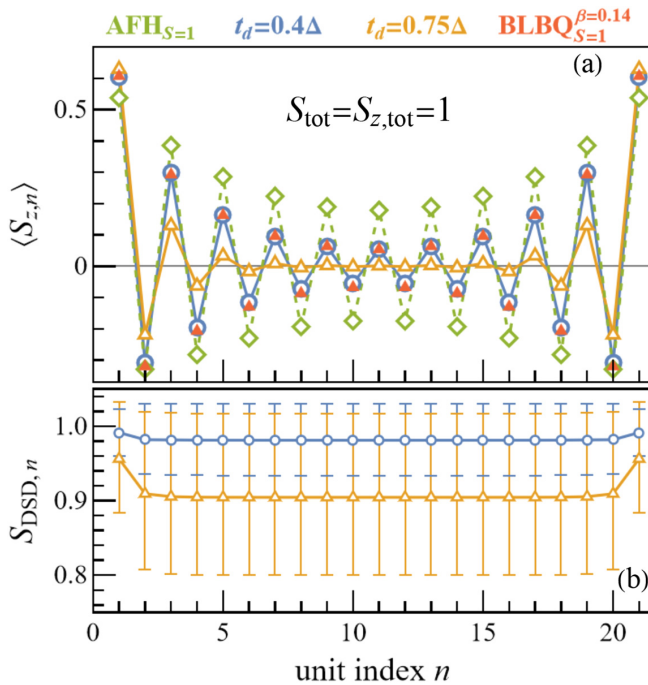


FIG. 5. (a) Average spin $\langle S_z \rangle$ along the $N = 21$ DSD, AFH, and BLBQ($\beta = 0.14$) chains in the $S_{\text{tot}} = S_{z,\text{tot}} = 1$ ground state. (b) Effective total spin $S_{\text{DSD},n}$ defined for each DSD unit $n = 1, \dots, 21$ by $S_{\text{DSD}}(S_{\text{DSD}} + 1) = \langle \tilde{S}_{\text{DSD}}^2 \rangle$, together with its estimated fluctuation range. The other parameters are $U = -2\epsilon_d = 6\Delta$, $\Gamma = 3\Delta$, $E_c = 2\Delta$. For the SI we employed the $\tilde{L} = 2$ surrogate.

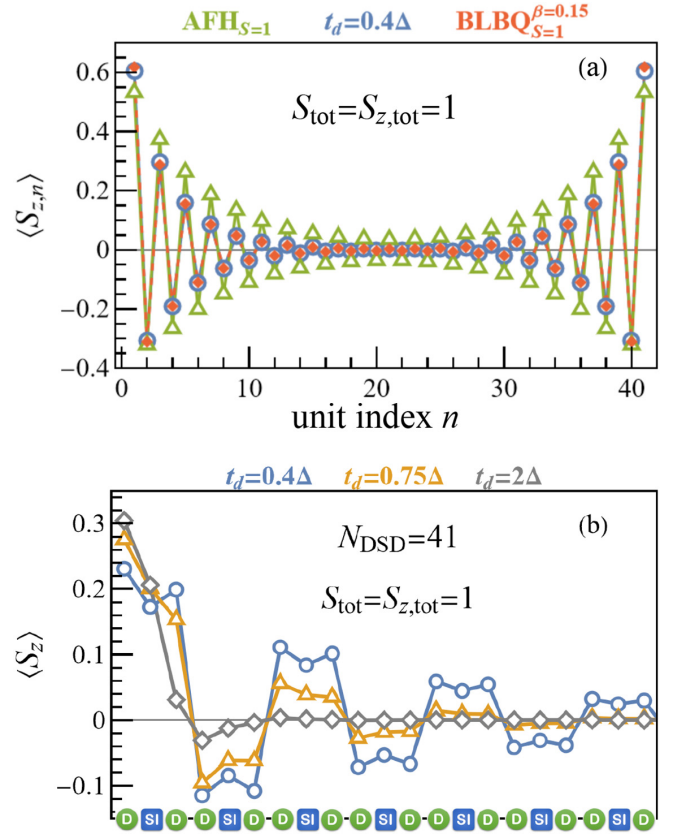


FIG. 6. (a) Average spin $\langle S_z \rangle$ along the $N = 41$ DSD, AFH, and BLBQ($\beta = 0.15$) chains in the $S_{\text{tot}} = S_{z,\text{tot}} = 1$ ground state. (b) Detailed average spin $\langle S_z \rangle$ for each QD and SI in the first seven units of the $N = 41$ DSD chain, in its $S_{\text{tot}} = S_{z,\text{tot}} = 1$ ground state, and for various interdot couplings t_d . The other parameters are $U = -2\epsilon_d = 6\Delta$, $\Gamma = 3\Delta$, $E_c = 2\Delta$. For each SI we employed the $\tilde{L} = 2$ surrogate.

projection $\langle S_z \rangle$ of a DSD unit. This is in agreement with the expectation from the previous analysis of a single DSD unit; see the discussion around Fig. 2. At large t_d , i.e., in the AKLT-like dimerized regime, the bulk average spin-density becomes strongly suppressed as all double-dots are tightly bound into spin-singlet dimers. What remains is an effective spin-1/2 moment localized on the outermost QD-SI block, with the individual QD and SI contributions close to their values in an isolated QD-SI system (around 0.3 and 0.2, respectively, for the chosen parameters).

3. String order parameters

The relatively long $N = 41$ chain features a bulk region large enough to accommodate a sound investigation of various correlation functions relevant to the Haldane phase; cf. Fig. 7. The correlators that are adequate here are string order parameters [23] of the form

$$g_{O,\mathcal{U}}(d) = \left\langle \hat{\mathcal{O}}_p \left(\prod_{j=p+1}^{p+d-1} \hat{\mathcal{U}}_j \right) \hat{\mathcal{O}}_{p+d} \right\rangle, \quad (8)$$

which probe the transformation behavior of the bulk under a symmetry \mathcal{U} , e.g., a spin rotation around the z axis with π , $R^z = \exp(i\pi S_z)$.

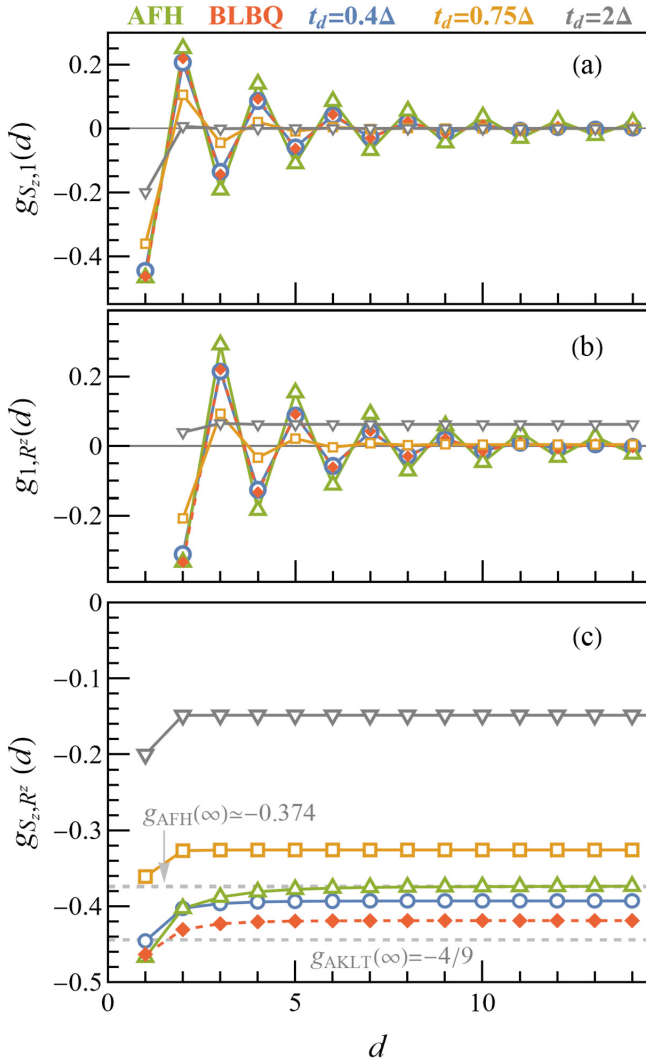


FIG. 7. (a) Average spin $\langle S_z \rangle$ along the $N = 41$ DSD, AFH, and BLBQ ($\beta = 0.15$) chains in the $S_{\text{tot}} = S_{z,\text{tot}} = 1$ ground state. (b)–(d) Correlation functions $g_{\mathcal{O}, \mathcal{U}}(d)$ of Eq. (8) for $\mathcal{O} = S_z$ and $\mathcal{U} = 1$ (b), $\mathcal{O} = 1$ and $\mathcal{U} = R^z$ (c), and $\mathcal{O} = S_z$ and $\mathcal{U} = R^z$ (d) in the bulk (middle third, $p = 14$) of the $N = 41$ chain. The other parameters are $U = -2\epsilon_d = 6\Delta$, $\Gamma = 3\Delta$, $E_c = 2\Delta$. For the SI we employed the $\tilde{L} = 2$ surrogate.

For $\mathcal{O} = S_z$ and $\mathcal{U} = 1$, Eq. (8) reduces to the spin-spin correlation function $g_{S_z, 1}(d) = \langle \hat{S}_{z,p} \hat{S}_{z,p+d} \rangle$, which is expected to be short-ranged as there is no spontaneous breaking of the rotational symmetry in the Haldane phase [21]. This behavior is confirmed in Fig. 7(a). The corresponding local correlation length may be estimated by $\xi = -1/\log[g_{S_z, 1}(d)/g_{S_z, 1}(d-1)]$, and is known to be $\xi_{\text{AFH}} \simeq 6$ and $\xi_{\text{AKLT}} = 1/\log 3 \simeq 0.9$ for the AFH and AKLT cases, respectively [28,64]. By computing $g_{S_z, 1}(d)$ for sites placed symmetrically around the middle of the chain, we obtain the estimates $\xi_{\text{DSD}} \simeq 3, 1.4$ and 0.5 for $t_d/\Delta = 0.4, 0.75$ and 2 , respectively. For $t_d/\Delta = 0.4, 0.75$ the correlation lengths thus interpolate between their AFH and AKLT counterparts. At a larger $t_d = 2\Delta$, where the DSD spin-1 character is mostly washed out, ξ_{DSD} drops below the AKLT value.

For $\mathcal{O} = 1$ and $\mathcal{U} = R^z$ one deals with the pure-string correlator g_{1, R^z} , which is nonzero at large d in the case of topologically trivial configurations [23]. In Fig. 7(b), as long as t_d is not too large, we find the pure-string correlator g_{1, R^z} to decay as expected for a Haldane phase where the bulk $\text{SO}(3)$ symmetry fractionalizes into the $\text{SU}(2)$ edge-symmetry. For the larger value $t_d = 2\Delta$, this pure-string correlator acquires a visibly finite positive value, signaling a trivial configuration.

The Haldane phase features a hidden antiferromagnetic order [65] that may be revealed by employing the nonlocal string order parameter g_{S_z, R^z} obtained from Eq. (8) upon setting $\mathcal{O} = S_z$ and $\mathcal{U} = R^z$ [23,66]. This may be viewed as a standard two-point spin-spin correlator that only picks up a \pm sign from the (nonlocally) alternating $S_z = \pm 1$ spins while ignoring all $S_z = 0$ contributions in between. Figure 7(c) shows that the DSD chain features a well-defined string order parameter, with a value close to its AFH and BLBQ counterparts for the moderate $t_d = 0.4\Delta$. With increasing t_d , we notice how the DSD string correlator $|g_{S_z, R^z}(\infty)|$ begins to decrease, e.g., reaching a significantly reduced value of 0.15 at $t_d = 2\Delta$ for which the above-mentioned pure-string correlator g_{1, R^z} also had long-range order.

When interpreting the order parameters' behavior, it is important to realize that an increasing interdot coupling t_d leads to the buildup of density fluctuations that gradually erode the spin-1 character of the DSD units. Strictly speaking, the original $\text{SO}(3)$ symmetry of an isolated spin-1 DSD unit is extended to $\text{SU}(2)$ at any finite t_d . At large t_d , the above string orders lose their distinguishing power, with g_{S_z, R^z} and g_{1, R^z} both acquiring a long-range order. Although the Haldane phase is adiabatically connected to a trivial state, its characteristic phenomena remain parametrically stable (i.e., over a large part of parameter space even when the bulk is in a trivial phase [67–69]).

In the remainder of this work, we will limit ourselves to the moderate value $t_d = 0.4\Delta$, which shows clear signatures of the Haldane phase.

4. Entanglement entropy

Even in the absence of string order parameters, topological phases can be characterized by their “entanglement spectrum” obtained upon performing a bipartite cut of the system, tracing out one part and diagonalizing the reduced density matrix of the other [70–73]. Below, we denote by λ_j the Schmidt eigenvalues that square to the eigenvalues of the reduced density matrix. In particular, the Haldane phases of integer spin chains are characterized by an even degeneracy of the entire entanglement spectrum, caused by the same symmetries protecting the stability of the Haldane phase when applied to the eigenstates of the reduced density matrix [74]. The computation of the entanglement spectrum is straightforward in our MPS approach, and leads to the results shown in Fig. 8. All chains under investigation (DSD, AFH, and BLBQ) consistently display the even degeneracy required by the Haldane phase (up to minute finite-size effects), and perfectly agree on the dominant pair of eigenvalues. While the higher-lying portions of the AFH and BLBQ's spectra naturally agree on the degeneracy patterns, some deviations occur for the DSD chain due to its underlying microscopic structure. This

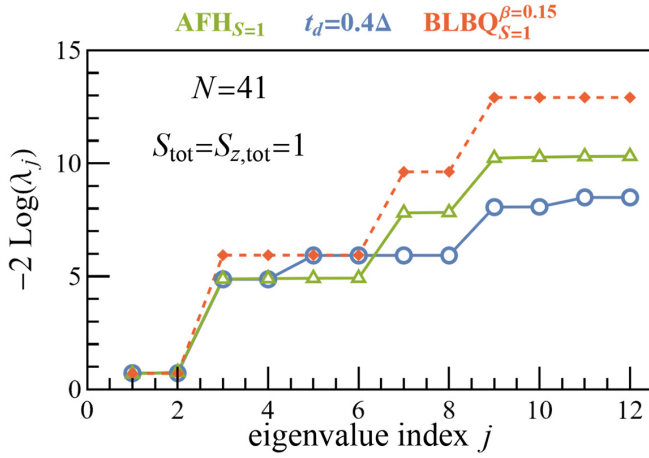


FIG. 8. Entanglement spectrum for a bipartition into $(N_L, N_R) = (20, 21)$ of the $N = 41$ DSD, AFH, and BLBQ chains in the $S_{\text{tot}} = S_{z,\text{tot}} = 1$ ground state. The DSD parameters are $U = -2\epsilon_d = 6\Delta$, $\Gamma = 3\Delta$, $E_c = 2\Delta$, $t_d = 0.4\Delta$ (a) and $t_d = 0.75\Delta$ (b). For the SI we employed the $\tilde{L} = 2$ surrogate.

is to be expected as the entanglement spectrum is a highly sensitive measure of a state's correlations. The corresponding entanglement entropies, computed as $S = -\sum_j \lambda_j^2 \log \lambda_j^2$, are $S_{\text{DSD}} = 0.857$, $S_{\text{AFH}} = 0.855$, $S_{\text{BLBQ}} = 0.760$ for Fig. 8(a).

5. Excited states

We end this section by examining how well the mapping of the DSD chain onto the ideal AFH and BLBQ models extends beyond the ground-state manifold. In Fig. 9, we show the magnetization profile of the lowest-lying $S = 2$ state in our longest $N = 21$ and 41 chains. All models agree well on the familiar staggered profile giving rise to the two edge-spins-1/2, and also on the bulk acquiring a quasiuniform spin density (responsible for the spin-1 magnon excitation). The only noticeable quantitative discrepancy is related to the DSD staggered profile extending slightly more into the bulk than in the case of the AFH or BLBQ. While higher-order corrections such as bicubic exchange couplings could be considered towards reaching a better quantitative agreement of an ideal $S = 1$ chain with the DSD chain, this is well beyond the scope of this work.

IV. CONCLUSIONS

The main purpose of this work was to show that the Haldane phase may be realized in a superconductor-semiconductor hybrid platform, more precisely in a chain of repeating QD-SI-QD (DSD) blocks, each exhibiting a robust spin-1 character over a sizable parameter regime. As long as the coupling between neighboring DSD units was not too strong to destroy their spin-1 character, the basic physics of the DSD chain could be quite well fitted by the bilinear-biquadratic spin-1 Hamiltonian of Eq. (7) with a biquadratic coefficient $\beta \in (0, 1/3)$. In this regime, the DSD chain was found to exhibit clear signatures of the Haldane phase, such as the presence of characteristic spin-density profiles with effective spins-1/2 at the edges, the long-range order of specific

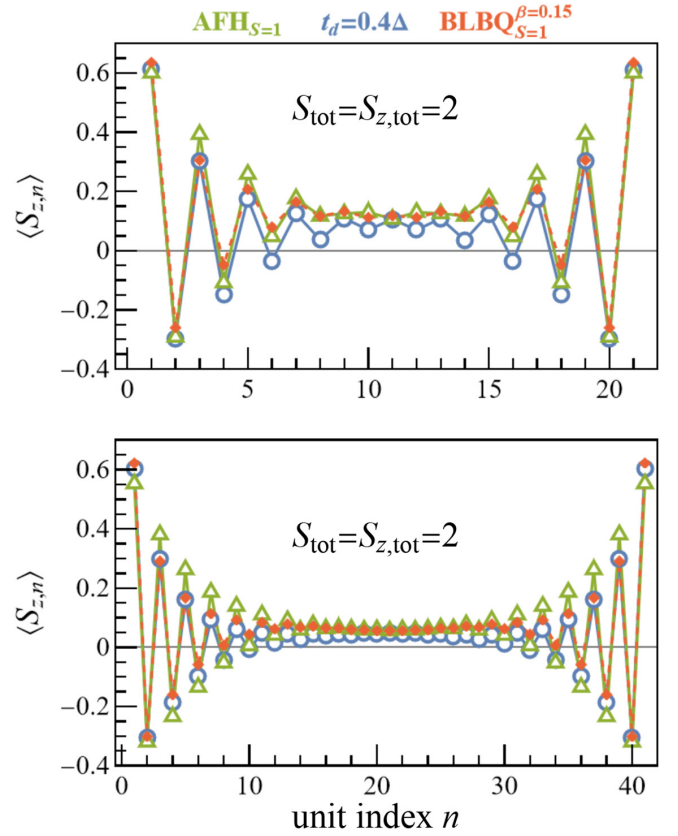


FIG. 9. Same as in Figs. 5(a) and 7(a), but for the lowest $S_{\text{tot}} = S_{z,\text{tot}} = 2$ excited state.

string correlation functions, and the double-degeneracy of the entanglement spectrum.

Our model could be extended, for example, by including an external magnetic field in order to define a singlet-triplet qubit protected from decoherence by a Haldane gap [38]. In this regime, our DSD unit would be closely related to the setup used in Ref. [13] to create poor man's Majorana states; it would thus be interesting to explore a possible crossover between the Haldane and Majorana physics in these systems. Furthermore, considering the effects of a spin-orbit interaction in the QDs, one could envision a realization of more general spin chains with anisotropic interactions, known to foster symmetry-protected topological phases beyond the Haldane phase [75].

One of the main advantages of the present super-semi platform lies in the ease of designing higher-spin units: by individually tunnel-coupling a number \mathcal{N} of QDs to the same SI, we would obtain a robust spin $S = \mathcal{N}/2$ unit [20]. This could enable the realization of more general spin models in various geometries [76]. In particular, the generalization of the AKLT state to spins-3/2 on a hexagonal lattice has notable implications for quantum computation [77,78]. However, the Heisenberg model on this lattice exhibits Néel order and is not in the same phase as the AKLT model [79], but a more general bilinear-biquadratic-bicubic model may actually be tuned to an AKLT phase [80]. In this context, it would be worthwhile to investigate how the present work generalizes to the analogous QD³-SI hexagonal network depicted in Fig. 10.

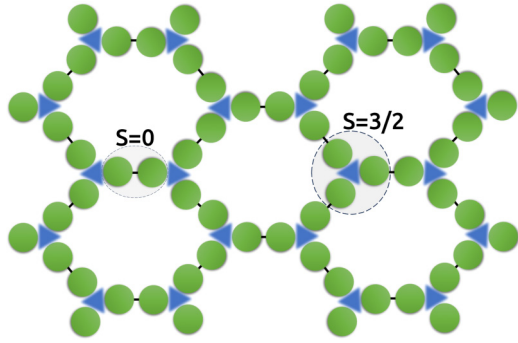


FIG. 10. Illustrations of the spin-3/2 QD³-SI honeycomb lattice. The QDs (SIs) are indicated green dots (blue triangles).

ACKNOWLEDGMENTS

We thank M. Burrello, K. Flensberg, and R. S. Souto for stimulating discussions and suggestions. This work was supported by a grant of the Romanian Ministry of Education and Research, Project No. 760122/31.07.2023 within PNRR-III-C9-2022-19.

APPENDIX A: QD-SI-QD PERTURBATION THEORY

We provide here additional insights from perturbation theory regarding the spin-singlet-triplet competition in the QD-SI-QD system. For a complementary picture, see also Appendix D of Ref. [19]. Our discussion below will parallel that of Sec. III A in Ref. [57].

For simplicity, we work here in the equivalent BCS picture obtained after transferring the charging term from the SI to the QDs; see Ref. [20] for details. As in the main text, we assume that the superconductor is described by an $\tilde{L} = 2$ surrogate with both levels coupled to each QD by the same tunneling amplitude t . We denote the quasiparticle energy by $E_{\text{qp}} = \sqrt{\Delta^2 + \xi^2}$, with $\xi = \xi_1 = -\xi_2 > 0$ indicating the levels' positions. For convenience we employ the BCS coherence factors u, v satisfying $uv = \Delta/2E_{\text{qp}}$, $u^2 - v^2 = \xi/E_{\text{qp}} > 0$.

Straightforward fourth-order nondegenerate perturbation theory in the tunnel coupling t (implemented for each total spin subspace using the SNEG software [81,82]) leads to the spin-singlet-triplet gap

$$\begin{aligned} \delta_{S-T} &\equiv \frac{E_{S=1} - E_{S=0}}{t^4} \\ &= \frac{16}{(U/2 + E_{\text{qp}} + E_c)^2(U + 2E_{\text{qp}} + 4E_c)} \\ &\quad + \frac{64u^2v^2}{(U/2 + E_{\text{qp}} + E_c)^2(U + 4E_c)} \\ &\quad + \frac{64u^2v^2}{(U/2 + E_{\text{qp}} + E_c)^2(U + 2E_{\text{qp}})} \\ &\quad - \frac{16(u^2 - v^2)^2}{(U/2 + E_{\text{qp}} + E_c)^2 2E_{\text{qp}}}. \end{aligned} \quad (\text{A1})$$

The perturbative expansion may be visualized in terms of spin-exchange processes with the matrix element of each process being weighted by the inverse product of the virtual excitation energies. A final state with exchanged spins may

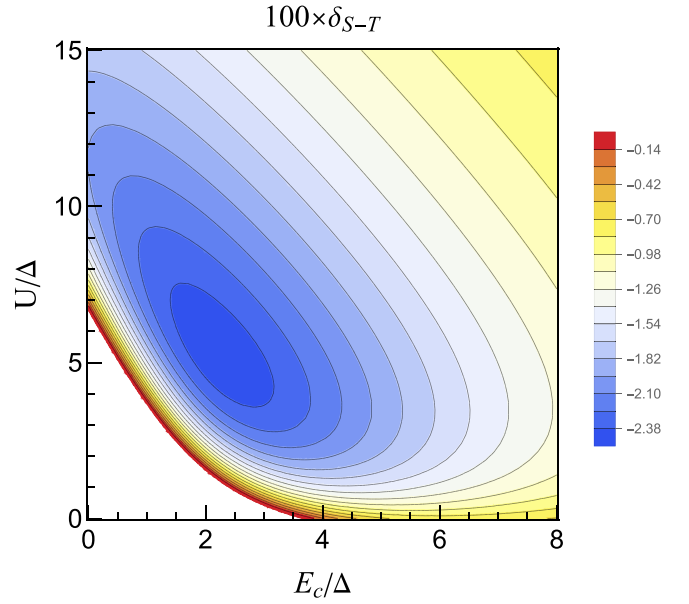


FIG. 11. Spin-singlet-triplet gap of Eq. (A1) vs U and E_c . The other parameters are $\Delta = 1$, $\epsilon_d = -U/2$, $\xi = 1.31\Delta$. Only the region with a spin-triplet ground state is colored.

be reached via intermediate virtual states connected by four tunneling events between the QDs and the superconductor.

In processes that involve only virtual excitations on the QDs, the two initial electrons have to be swapped, leading to an overall sign that energetically favors the spin-singlet state. This is the case for the first three terms in Eq. (A1). It is possible, however, to also exchange the spins without anticommutation signs through processes in which a hole is involved. These kinds of processes will energetically favor the spin-triplet state, leading to the appearance of the last term in Eq. (A1).

The ratio between triplet-favoring and singlet-favoring processes is given schematically by $1 + E_{\text{QDs}}/E_{\text{qp}}$, where $E_{\text{QDs}} \sim U + E_c$ is a typical excitation energy in the QD subsystem. When it becomes advantageous to perform the spin-exchange by virtually exciting the superconductor instead of the QDs, a spin-triplet ground state may emerge.

Notice, however, that there is a certain amount of destructive interference in the last term of Eq. (A1). Namely, its subset of processes involving all possible excitations on both superconducting levels (of the type $u_1 v_1 u_2 v_2 = u^2 v^2$) will favor the spin-singlet instead. This effect completely suppresses the last term of Eq. (A1) in the zero-bandwidth limit of degenerate levels $\xi = 0$: for the spin-triplet to be the ground state, at least two distinct levels with enough separation are required in the superconductor.

Finally, we consider the large- U limit

$$\delta_{S-T} = -\frac{32\xi^2}{U^2 E_{\text{qp}}^3} + \frac{64(3 + 2E_c \xi^2/E_{\text{qp}}^3)}{U^3} + O(U^{-4}) \quad (\text{A2})$$

and the large- E_c limit

$$\delta_{S-T} = \frac{8}{E_c^2} \left[-\frac{\xi^2}{E_{\text{qp}}^3} + \frac{2\Delta^2}{E_{\text{qp}}^2(U + 2E_{\text{qp}})} \right] + O(E_c^{-3}), \quad (\text{A3})$$

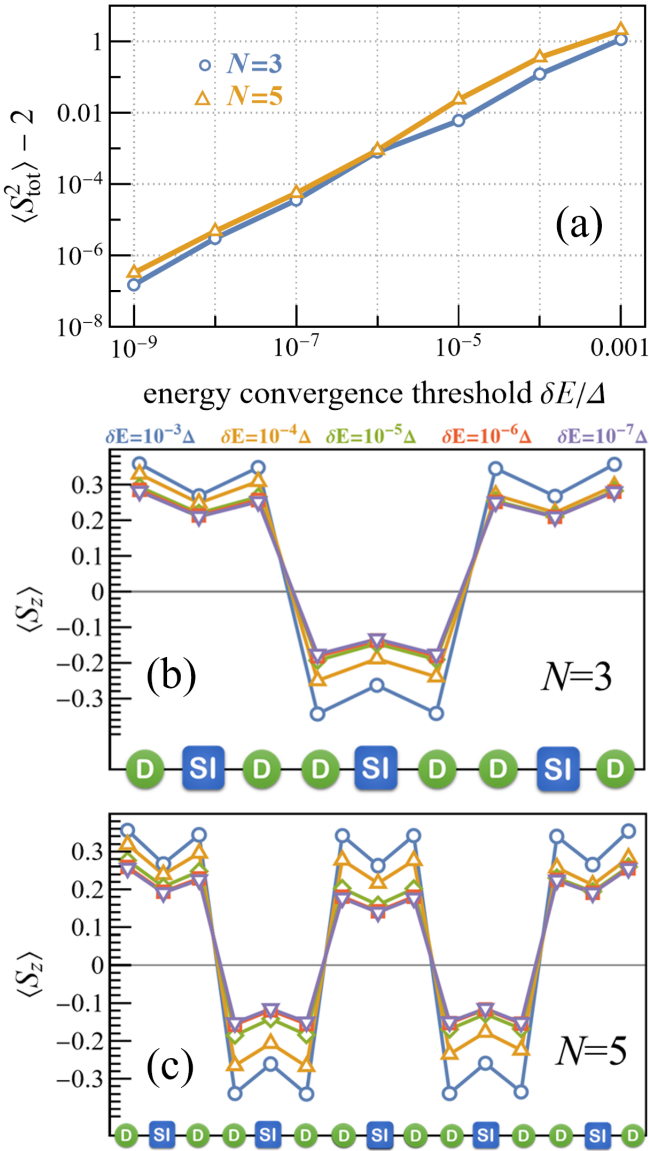


FIG. 12. (a) Deviation of the total spin from its exact value, $\langle \hat{S}_{\text{tot}}^2 \rangle - 2$, vs the DMRG energy convergence threshold δE , for the spin-triplet ground states of the $N = 3, 5$ DSD chains. (b), (c) Ground-state average spin $\langle S_z \rangle$ along the $N = 3, 5$ DSD chains for various energy convergence thresholds $\delta E = 10^{-3}\Delta - 10^{-7}\Delta$. The DSD chain parameters are $U = -2\epsilon_d = 6\Delta$, $\Gamma = 3\Delta$, $E_c = 2\Delta$, $t_d = 0.4\Delta$. For each SI we employed the $\tilde{L} = 2$ surrogate.

which are both in agreement with the above considerations (and with the conclusions of Ref. [19]) regarding the existence of a finite bandwidth threshold for establishing the spin-triplet ground state. Note, however, that the numerical examples considered in the main text (with $U = 6\Delta$, $E_c = 2\Delta$) do not fall under any of these limits, but are chosen instead to ensure the maximum spin-singlet-triplet gap; see Fig. 11.

APPENDIX B: DMRG TECHNICAL DETAILS

We collect in this Appendix the technical details regarding our DMRG simulations. The latter are based on the ITensor

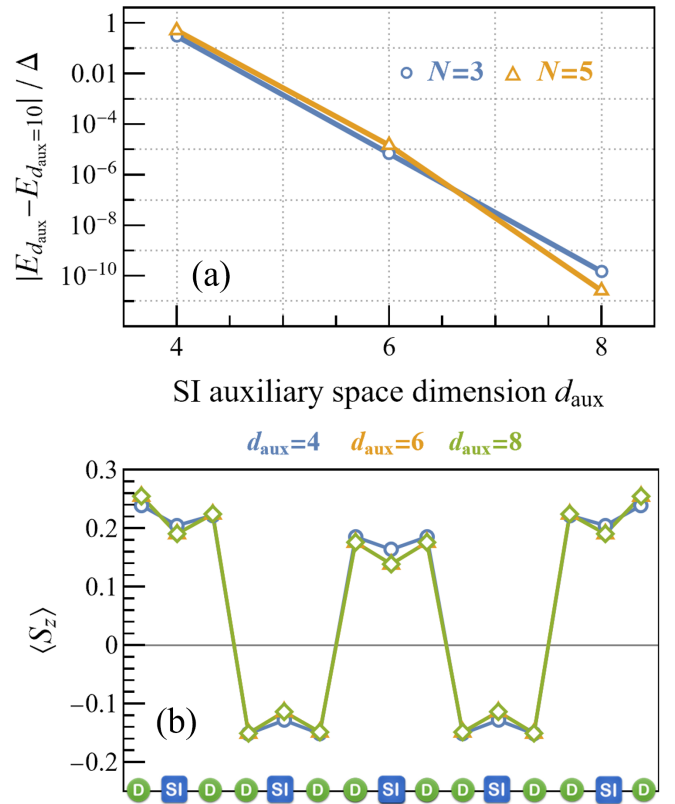


FIG. 13. (a) Ground-state energy loss for various SI auxiliary space dimensions $d_{\text{aux}} = 4, 6, 8$, relative to the $d_{\text{aux}} = 10$ value. (b) Corresponding ground-state average spin $\langle S_z \rangle$ along the $N = 5$ DSD chain, for $d_{\text{aux}} = 4, 6, 8$. The DSD chain parameters are $U = -2\epsilon_d = 6\Delta$, $\Gamma = 3\Delta$, $E_c = 2\Delta$, $t_d = 0.4\Delta$. For each SI we employed the $\tilde{L} = 2$ surrogate.

library [83,84], which allows us to seamlessly combine various kinds of local Hilbert spaces, e.g., fermionic and auxiliary spaces for each SI. Our numerical codes are available online [85] and may be run on a standard laptop or desktop computer.

In obtaining the results presented in the main text, we employed a maximum MPS bond dimension of 2000, a singular value truncation cutoff of 10^{-13} , and we made use of the ITensor noise term for aiding convergence. We used an energy convergence threshold of $\delta E = 5 \times 10^{-9}\Delta$ and we truncated the auxiliary Hilbert space for each SI to the dimension $d_{\text{aux}} = 10$.

While the ITensor library does allow for the conservation of locally additive quantum numbers, e.g., the total spin component $S_{z,\text{tot}}$ and the total particle number N_{tot} , it does not currently support enforcing global non-Abelian symmetries like the $SU(2)$ total spin invariance. This is not an issue for even-length DSD chains, where minimizing $\langle \hat{H} \rangle$ in a given $S_{z,\text{tot}}$ sector leads to the corresponding $|S_{\text{tot}} = S_{z,\text{tot}}\rangle$ state. However, in computing the first excited spin-singlet state in odd-length DSD chains, a naive $\langle \hat{H} \rangle$ minimization in the $S_{z,\text{tot}} = 0$ sector would yield the $|S_{\text{tot}} = 1, S_{z,\text{tot}} = 0\rangle$ component of the spin-triplet ground multiplet. To remedy this situation, we perform the minimization of $\langle \hat{H} + w\hat{S}_{\text{tot}}^2 \rangle$, where \hat{S}_{tot}^2 is the total spin operator [19]. When the weight w exceeds the spin-singlet-triplet gap, the extra term penalizes

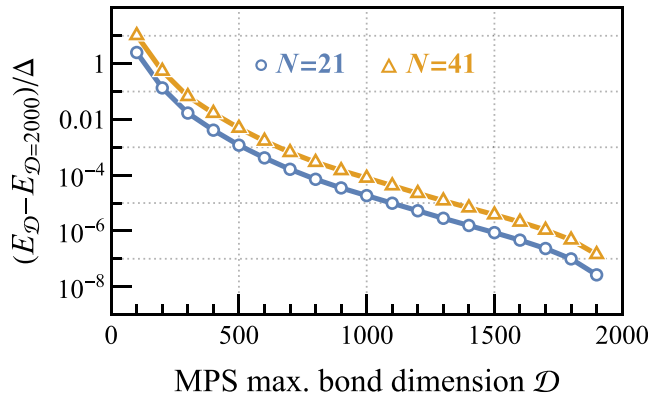


FIG. 14. Energy variation obtained by truncating the ground-state MPS down to various bond dimensions \mathcal{D} , relative to the original $\mathcal{D} = 2000$ value, for the $N = 21, 41$ DSD chains. The DSD chain parameters are $U = -2\epsilon_d = 6\Delta$, $\Gamma = 3\Delta$, $E_c = 2\Delta$, $t_d = 0.4\Delta$. For each SI we employed the $\tilde{L} = 2$ surrogate.

the spin-triplet enough to allow for the spin-singlet to be found by the minimization.

In our simulations, the total spin is thus not a conserved quantity, and its correct value is achieved only asymptotically in the energy minimization process, as the contributions of the excited states are systematically eliminated. This is illustrated in Fig. 12(a), where for the $S_{\text{tot}} = 1$ ground state of

the $N = 3, 5$ DSD chains, we obtain $\langle \hat{S}_{\text{tot}}^2 \rangle - 2 \sim 1000 \delta E / \Delta$, requiring quite a low-energy threshold δE to achieve good convergence. This is reflected also in the spin-density profiles along the chains shown in Figs. 12(b) and 12(c), which converge well only below $\delta E / \Delta \sim 10^{-5} - 10^{-6}$.

On the other hand, convergence with respect to increasing the SI auxiliary space dimension d_{aux} is achieved much more rapidly. Given the relatively large charging energy $E_c = 2\Delta$ chosen in our simulations, a relatively small value of $d_{\text{aux}} \sim 6-8$ is able to safely account for all relevant SI charge fluctuations; see Fig. 13.

Finally, let us discuss the effects of truncating the MPS ground states for the longest chains analyzed in this work, $N = 21, 41$. We show in Fig. 14 the energy variation $\langle \hat{H} \rangle_{\mathcal{D}} - \langle \hat{H} \rangle_{\mathcal{D}=2000}$ obtained upon truncating the two MPSs down to various bond dimensions $100 \leq \mathcal{D} \leq 1900$, relative to the actual value used in the energy optimization process $\mathcal{D} = 2000$. This also provides an upper bound for the energy variations that would be obtained by actually performing various DMRG minimizations at smaller bond dimensions. Figure 14 confirms that convergence has been satisfactorily achieved at $\mathcal{D} = 2000$, with $(\langle \hat{H} \rangle_{\mathcal{D}=1900} - \langle \hat{H} \rangle_{\mathcal{D}=2000}) / \Delta \sim 10^{-7} - 10^{-8}$ for $N = 21, 41$.

As a complementary convergence indicator for the large-scale $N = 21, 41$ calculations, let us mention the errors in the ground-state total spin (at $\mathcal{D} = 2000$), i.e., $\langle \hat{S}_{\text{tot}}^2 \rangle - 2 = 2.7 \times 10^{-6}$ and 1.3×10^{-6} , respectively, in good agreement with Fig. 12 given the energy convergence threshold $\delta E = 5 \times 10^{-9} \Delta$ considered here.

[1] J. Bauer, A. Oguri, and A. C. Hewson, Spectral properties of locally correlated electrons in a Bardeen–Cooper–Schrieffer, *J. Phys.: Condens. Matter* **19**, 486211 (2007).
[2] T. Meng, S. Florens, and P. Simon, Self-consistent description of Andreev bound states in Josephson quantum dot devices, *Phys. Rev. B* **79**, 224521 (2009).
[3] A. Oguri, Y. Tanaka, and J. Bauer, Interplay between Kondo and Andreev–Josephson effects in a quantum dot coupled to one normal and two superconducting leads, *Phys. Rev. B* **87**, 075432 (2013).
[4] Y. Luh, Bound state in superconductors with paramagnetic impurities, *Acta Phys. Sin.* **21**, 75 (1965).
[5] H. Shiba, Classical spins in superconductors, *Prog. Theor. Phys.* **40**, 435 (1968).
[6] A. I. Rusinov, Superconductivity near a paramagnetic impurity, *JETP Lett.* **9**, 85 (1969) [*Zh. Eksp. Teor. Fiz.* **9**, 146 (1968)].
[7] G. Kiršanskas, M. Goldstein, K. Flensberg, L. I. Glazman, and J. Paaske, Yu–Shiba–Rusinov states in phase-biased superconductor–quantum dot–superconductor junctions, *Phys. Rev. B* **92**, 235422 (2015).
[8] A. Mishra, P. Simon, T. Hyart, and M. Trif, Yu–Shiba–Rusinov Qubit, *PRX Quantum* **2**, 040347 (2021).
[9] L. Pavešić and R. Žitko, Qubit based on spin-singlet Yu–Shiba–Rusinov states, *Phys. Rev. B* **105**, 075129 (2022).
[10] M. Pita-Vidal, A. Bargerbos, R. Žitko, L. J. Splitthoff, L. Grünhaupt, J. J. Wesdorp, Y. Liu, L. P. Kouwenhoven, R. Aguado, B. van Heck, A. Kou, and C. K. Andersen, Direct

manipulation of a superconducting spin qubit strongly coupled to a transmon qubit, *Nat. Phys.* **19**, 1110 (2023).

[11] M. Leijnse and K. Flensberg, Parity qubits and poor man’s Majorana bound states in double quantum dots, *Phys. Rev. B* **86**, 134528 (2012).
[12] J. D. Sau and S. D. Sarma, Realizing a robust practical Majorana chain in a quantum-dot–superconductor linear array, *Nat. Commun.* **3**, 964 (2012).
[13] A. Tsintzis, R. S. Souto, and M. Leijnse, Creating and detecting poor man’s Majorana bound states in interacting quantum dots, *Phys. Rev. B* **106**, L201404 (2022).
[14] C.-X. Liu, G. Wang, T. Dvir, and M. Wimmer, Tunable superconducting coupling of quantum dots via Andreev bound states in semiconductor–superconductor nanowires, *Phys. Rev. Lett.* **129**, 267701 (2022).
[15] T. Dvir, G. Wang, N. van Loo, C.-X. Liu, G. P. Mazur, A. Bordin, S. L. D. Ten Haaf, J.-Y. Wang, D. van Driel, F. Zatelli, X. Li, F. K. Malinowski, S. Gazibegovic, G. Badawy, E. P. A. M. Bakkers, M. Wimmer, and L. P. Kouwenhoven, Realization of a minimal Kitaev chain in coupled quantum dots, *Nature (London)* **614**, 445 (2023).
[16] F. Zatelli, D. van Driel, D. Xu, G. Wang, C.-X. Liu, A. Bordin, B. Roovers, G. P. Mazur, N. van Loo, J. C. Wolff, A. M. Bozkurt, G. Badawy, S. Gazibegovic, E. P. A. M. Bakkers, M. Wimmer, L. P. Kouwenhoven, and T. Dvir, Robust poor man’s Majorana zero modes using Yu–Shiba–Rusinov states, [arXiv:2311.03193](https://arxiv.org/abs/2311.03193).

- [17] A. Tsintzis, R. S. Souto, K. Flensberg, J. Danon, and M. Leijnse, Majorana qubits and non-Abelian physics in quantum dot-based minimal Kitaev chains, *PRX Quantum* **5**, 010323 (2024).
- [18] A. Bordin, C.-X. Liu, T. Dvir, F. Zatelli, S. L. D. t. Haaf, D. van Driel, G. Wang, N. van Loo, T. van Caekenberghe, J. C. Wolff, Y. Zhang, G. Badawy, S. Gazibegovic, E. P. A. M. Bakkers, M. Wimmer, L. P. Kouwenhoven, and G. P. Mazur, Signatures of Majorana protection in a three-site Kitaev chain, [arXiv:2402.19382](https://arxiv.org/abs/2402.19382).
- [19] Á. Bácsi, L. Pavešić, and R. Žitko, Exchange interaction between two quantum dots coupled through a superconducting island, *Phys. Rev. B* **108**, 115160 (2023).
- [20] V. V. Baran and J. Paaske, BCS surrogate models for floating superconductor-semiconductor hybrids, *Phys. Rev. B* **109**, 224501 (2024).
- [21] F. D. M. Haldane, Continuum dynamics of the 1-D Heisenberg antiferromagnet: Identification with the $O(3)$ nonlinear sigma model, *Phys. Lett. A* **93**, 464 (1983).
- [22] F. D. M. Haldane, Nonlinear field theory of large-spin Heisenberg antiferromagnets: Semiclassically quantized solitons of the one-dimensional easy-axis Néel state, *Phys. Rev. Lett.* **50**, 1153 (1983).
- [23] F. Pollmann, E. Berg, A. M. Turner, and M. Oshikawa, Symmetry protection of topological phases in one-dimensional quantum spin systems, *Phys. Rev. B* **85**, 075125 (2012).
- [24] F. D. M. Haldane, Nobel lecture: Topological quantum matter, *Rev. Mod. Phys.* **89**, 040502 (2017).
- [25] X.-G. Wen, *Colloquium: Zoo of quantum-topological phases of matter*, *Rev. Mod. Phys.* **89**, 041004 (2017).
- [26] X. Chen, Z.-C. Gu, and X.-G. Wen, Classification of gapped symmetric phases in one-dimensional spin systems, *Phys. Rev. B* **83**, 035107 (2011).
- [27] I. Affleck, T. Kennedy, E. H. Lieb, and H. Tasaki, Rigorous results on valence-bond ground states in antiferromagnets, *Phys. Rev. Lett.* **59**, 799 (1987).
- [28] S. R. White and D. A. Huse, Numerical renormalization-group study of low-lying eigenstates of the antiferromagnetic $S=1$ Heisenberg chain, *Phys. Rev. B* **48**, 3844 (1993).
- [29] T. Jolicoeur and O. Golinelli, Physics of integer-spin antiferromagnetic chains: Haldane gaps and edge states, *Comptes Rendus. Chim.* **22**, 445 (2019).
- [30] E. H. Kim, G. Fáth, J. Sólyom, and D. J. Scalapino, Phase transitions between topologically distinct gapped phases in isotropic spin ladders, *Phys. Rev. B* **62**, 14965 (2000).
- [31] I. A. Zaliznyak, S.-H. Lee, and S. V. Petrov, Continuum in the spin-excitation spectrum of a Haldane chain observed by neutron scattering in CsNiCl_3 , *Phys. Rev. Lett.* **87**, 017202 (2001).
- [32] M. Kenzelmann, R. A. Cowley, W. J. L. Buyers, Z. Tun, R. Coldea, and M. Enderle, Properties of Haldane excitations and multiparticle states in the antiferromagnetic spin-1 chain compound CsNiCl_3 , *Phys. Rev. B* **66**, 024407 (2002).
- [33] M. Kenzelmann, G. Xu, I. A. Zaliznyak, C. Broholm, J. F. DiTusa, G. Aeppli, T. Ito, K. Oka, and H. Takagi, Structure of end states for a Haldane spin chain, *Phys. Rev. Lett.* **90**, 087202 (2003).
- [34] P. Sompert, S. Hirthe, D. Bourgund, T. Chalopin, J. Bibo, J. Koepsell, P. Bojović, R. Verresen, F. Pollmann, G. Salomon, C. Gross, T. A. Hilker, and I. Bloch, Realizing the symmetry-protected Haldane phase in Fermi-Hubbard ladders, *Nature (London)* **606**, 484 (2022).
- [35] A. Nag, A. Nocera, S. Agrestini, M. Garcia-Fernandez, A. C. Walters, S.-W. Cheong, S. Johnston, and K.-J. Zhou, Quadrupolar magnetic excitations in an isotropic spin-1 antiferromagnet, *Nat. Commun.* **13**, 1 (2022).
- [36] P. Jelínek, Quantum spin chains go organic, *Nat. Chem.* **15**, 12 (2023).
- [37] Y.-P. Shim, A. Sharma, C.-Y. Hsieh, and P. Hawrylak, Artificial Haldane gap material on a semiconductor chip, *Solid State Commun.* **150**, 2065 (2010).
- [38] B. Jaworowski, N. Rogers, M. Grabowski, and P. Hawrylak, Macroscopic singlet-triplet qubit in synthetic spin-one chain in semiconductor nanowires, *Sci. Rep.* **7**, 5529 (2017).
- [39] J. Manalo, M. Cygorek, A. Altintas, and P. Hawrylak, Electronic and magnetic properties of many-electron complexes in charged $\text{InAs}_x\text{P}_{1-x}$ quantum dots in InP nanowires, *Phys. Rev. B* **104**, 125402 (2021).
- [40] J. Manalo, D. Miravet, and P. Hawrylak, Microscopic design of a synthetic spin-1 chain in an InAsP quantum dot array, *Phys. Rev. B* **109**, 085112 (2024).
- [41] S. Mishra, G. Catarina, F. Wu, R. Ortiz, D. Jacob, K. Eimre, J. Ma, C. A. Pignedoli, X. Feng, P. Ruffieux, J. Fernández-Rossier, and R. Fasel, Observation of fractional edge excitations in nanographene spin chains, *Nature (London)* **598**, 287 (2021).
- [42] G. Catarina and J. Fernández-Rossier, Hubbard model for spin-1 Haldane chains, *Phys. Rev. B* **105**, L081116 (2022).
- [43] R. C. Williams, W. J. A. Blackmore, S. P. M. Curley, M. R. Lees, S. M. Birnbaum, J. Singleton, B. M. Huddart, T. J. Hicken, T. Lancaster, S. J. Blundell, F. Xiao, A. Ozarowski, F. L. Pratt, D. J. Voneshen, Z. Guguchia, C. Baines, J. A. Schlueter, D. Y. Villa, J. L. Manson, and P. A. Goddard, Near-ideal molecule-based Haldane spin chain, *Phys. Rev. Res.* **2**, 013082 (2020).
- [44] W. Zheng, C. J. Hamer, and R. R. P. Singh, Spectral properties of alternating antiferromagnetic-ferromagnetic spin-half chains and the emergence of composite spin-one behavior, *Phys. Rev. B* **74**, 172407 (2006).
- [45] M. B. Stone, W. Tian, M. D. Lumsden, G. E. Granroth, D. Mandrus, J.-H. Chung, N. Harrison, and S. E. Nagler, Quantum spin correlations in an organometallic alternating-sign chain, *Phys. Rev. Lett.* **99**, 087204 (2007).
- [46] J. Pitcairn, A. Iliceto, L. Cañadillas-Delgado, O. Fabelo, C. Liu, C. Balz, A. Weilhard, S. P. Argent, A. J. Morris, and M. J. Cliffe, Low-dimensional metal-organic magnets as a route toward the $S=2$ Haldane phase, *J. Am. Chem. Soc.* **145**, 1783 (2023).
- [47] P. Tin, M. J. Jenkins, J. Xing, N. Caci, Z. Gai, R. Jin, S. Wessel, J. Krzystek, C. Li, L. L. Daemen, Y. Cheng, and Z.-L. Xue, Haldane topological spin-1 chains in a planar metal-organic framework, *Nat. Commun.* **14**, 5454 (2023).
- [48] B. Jaworowski and P. Hawrylak, Quantum bits with macroscopic topologically protected states in semiconductor devices, *Appl. Sci.* **9**, 474 (2019).
- [49] A. Miyake, Quantum computation on the edge of a symmetry-protected topological order, *Phys. Rev. Lett.* **105**, 040501 (2010).
- [50] S. D. Bartlett, G. K. Brennen, A. Miyake, and J. M. Renes, Quantum computational renormalization in the Haldane phase, *Phys. Rev. Lett.* **105**, 110502 (2010).
- [51] V. V. Baran, E. J. P. Frost, and J. Paaske, Surrogate model solver for impurity-induced superconducting subgap states, *Phys. Rev. B* **108**, L220506 (2023).

- [52] O. K urt ossy, M. Bod ocs, C. P. Moca, Z. Scher ubl, E. Nikodem, T. Kanne, J. Nyg ard, G. Zar and, P. Makk, and S. Csonka, Heteroatomic Andreev molecule in a superconducting island-double quantum dot hybrid, [arXiv:2407.00825](#).
- [53] P. W. Anderson, New approach to the theory of superexchange interactions, *Phys. Rev.* **115**, 2 (1959).
- [54] T. Kennedy, Exact diagonalisations of open spin-1 chains, *J. Phys.: Condens. Matter* **2**, 5737 (1990).
- [55] S. R. White, Density matrix formulation for quantum renormalization groups, *Phys. Rev. Lett.* **69**, 2863 (1992).
- [56] U. Schollw ock, The density-matrix renormalization group in the age of matrix product states, *Ann. Phys.* **326**, 96 (2011).
- [57] B. Probst, F. Dom inguez, A. Schroer, A. L. Yeyati, and P. Recher, Signatures of nonlocal Cooper-pair transport and of a singlet-triplet transition in the critical current of a double-quantum-dot Josephson junction, *Phys. Rev. B* **94**, 155445 (2016).
- [58] C. J unger, A. Baumgartner, R. Delagr ange, D. Chevallier, S. Lehmann, M. Nilsson, K. A. Dick, C. Thelander, and C. Sch onenberger, Spectroscopy of the superconducting proximity effect in nanowires using integrated quantum dots, *Commun. Phys.* **2**, 1 (2019).
- [59] F. S. Thomas, A. Baumgartner, L. Gubser, C. J unger, G. F ul op, M. Nilsson, F. Rossi, V. Zannier, L. Sorba, and C. Sch onenberger, Highly symmetric and tunable tunnel couplings in InAs/InP nanowire heterostructure quantum dots, *Nanotechnology* **31**, 135003 (2020).
- [60] J. H. Ungerer, A. Pally, A. Kononov, S. Lehmann, J. Ridderbos, P. P. Potts, C. Thelander, K. A. Dick, V. F. Maisi, P. Scarlino, A. Baumgartner, and C. Sch onenberger, Strong coupling between a microwave photon and a singlet-triplet qubit, *Nat. Commun.* **15**, 1068 (2024).
- [61] K. Hida, Crossover between the Haldane-gap phase and the dimer phase in the spin-1/2 alternating Heisenberg chain, *Phys. Rev. B* **45**, 2207 (1992).
- [62] K. Hida, Ground-state phase diagram of the spin 1/2 alternating Heisenberg chain with anisotropy on the antiferromagnetic bond, *J. Phys. Soc. Jpn.* **62**, 1463 (1993).
- [63] More precisely, we fitted the t_d^2 dependency of the DSD-dimer's spin-quintuplet-triplet gap for three different values of U , obtaining $J_{AF} = \gamma t_d^2 / U$ with the proportionality factor γ only showing a weak U dependence, $\gamma = 0.8, 0.9, 0.97$ for $U/\Delta = 3, 6, 10$.
- [64] I. Affleck, Quantum spin chains and the Haldane gap, *J. Phys.: Condens. Matter* **1**, 3047 (1989).
- [65] T. Kennedy and H. Tasaki, Hidden $Z_2 \times Z_2$ symmetry breaking in Haldane-gap antiferromagnets, *Phys. Rev. B* **45**, 304 (1992).
- [66] M. den Nijs and K. Rommelse, Preroughening transitions in crystal surfaces and valence-bond phases in quantum spin chains, *Phys. Rev. B* **40**, 4709 (1989).
- [67] F. Anfuso and A. Rosch, Fragility of string orders, *Phys. Rev. B* **76**, 085124 (2007).
- [68] S. Moudgalya and F. Pollmann, Fragility of symmetry-protected topological order on a Hubbard ladder, *Phys. Rev. B* **91**, 155128 (2015).
- [69] R. Verresen, J. Bibo, and F. Pollmann, Quotient symmetry protected topological phenomena, [arXiv:2102.08967](#).
- [70] H. Li and F. D. M. Haldane, Entanglement spectrum as a generalization of entanglement entropy: Identification of topological order in non-Abelian fractional quantum Hall effect states, *Phys. Rev. Lett.* **101**, 010504 (2008).
- [71] M. Levin and X.-G. Wen, Detecting topological order in a ground state wave function, *Phys. Rev. Lett.* **96**, 110405 (2006).
- [72] A. Kitaev and J. Preskill, Topological entanglement entropy, *Phys. Rev. Lett.* **96**, 110404 (2006).
- [73] A. M. Turner, Y. Zhang, and A. Vishwanath, Entanglement and inversion symmetry in topological insulators, *Phys. Rev. B* **82**, 241102(R) (2010).
- [74] F. Pollmann, A. M. Turner, E. Berg, and M. Oshikawa, Entanglement spectrum of a topological phase in one dimension, *Phys. Rev. B* **81**, 064439 (2010).
- [75] Z.-X. Liu, M. Liu, and X.-G. Wen, Gapped quantum phases for the $S = 1$ spin chain with D_{2h} symmetry, *Phys. Rev. B* **84**, 075135 (2011).
- [76] K. Ren, M. Wu, S.-S. Gong, D.-X. Yao, and H.-Q. Wu, Haldane phases and phase diagrams of the $S = \frac{3}{2}$ and $S = 1$ bilinear-biquadratic Heisenberg model on the orthogonal dimer chain, *Phys. Rev. B* **108**, 245104 (2023).
- [77] T.-C. Wei, I. Affleck, and R. Raussendorf, Affleck-Kennedy-Lieb-Tasaki state on a honeycomb lattice is a universal quantum computational resource, *Phys. Rev. Lett.* **106**, 070501 (2011).
- [78] T.-C. Wei, I. Affleck, and R. Raussendorf, Two-dimensional Affleck-Kennedy-Lieb-Tasaki state on the honeycomb lattice is a universal resource for quantum computation, *Phys. Rev. A* **86**, 032328 (2012).
- [79] C.-Y. Huang, M. A. Wagner, and T.-C. Wei, Emergence of XY-like phase in deformed spin- $\frac{3}{2}$ AKLT systems, *Phys. Rev. B* **94**, 165130 (2016).
- [80] C.-Y. Huang, X. Chen, and F.-L. Lin, Symmetry-protected quantum state renormalization, *Phys. Rev. B* **88**, 205124 (2013).
- [81] R.  zitko, SNEG – Mathematica package for symbolic calculations with second-quantization-operator expressions, *Comput. Phys. Commun.* **182**, 2259 (2011).
- [82] R.  zitko, rokzitko/sneg: April 2022 release (2024) [Online accessed 2 April 2024], doi:10.5281/zenodo.6470647.
- [83] M. Fishman, S. R. White, and E. M. Stoudenmire, The ITensor software library for tensor network calculations, *SciPost Phys. Codebases* **4** (2022).
- [84] M. Fishman, S. R. White, and E. M. Stoudenmire, Codebase release 0.3 for ITensor, *SciPost Phys. Codebases* **4** (2022).
- [85] V. V. Baran, Surrogate models GitHub repository, https://github.com/virgilb91/surrogate_models/tree/main.